ARTICLE

Tuning Molecular Adsorption in SBA-15-Type Periodic Mesoporous Organosilicas by Systematic Variation of their Surface Polarity†

Received 00th January 20xx,
Accepted 00th January 20xx

DOI: 10.1039/x0xx00000x

Hyunjin Moon,[a] Songi Han*[a,b] and Susannah L. Scott*[a,b]

Surface polarity plays a key role in controlling molecular adsorption at solid-liquid interfaces, with major implications for reactions and separations. In this study, the chemical composition of periodic mesoporous organosilicas (PMOs) was varied by co-condensing $Si(OEt)_4$ with organodisilanes, to create a homologous series of materials with similar surface areas, pore volumes, and hydroxyl contents. Their relative surface polarities, obtained by measuring the fluorescence of a solvatochromic dye, cover a wide range. The EPR spectra of PMO materials modified with tethered nitroxide radicals reveal monotonically decreasing mobility as more of the radicals interact strongly with the increasingly non-polar surface. The surface properties of the PMOs correlate with their affinities for organic molecules dissolved in various solvents. The most polar material has negligible affinity for organic molecules such as phenol, *p*-cresol, or furfural when they are dissolved in water. However, stronger solute-surface interactions make adsorption increasingly favorable as the surface polarity decreases. The trend is reversed for furfural in benzene, where weaker solvent–surface interactions result in higher adsorption on polar surfaces. In DMSO, furfural adsorption is suppressed due to the similar strengths of solute-surface and solvent–surface interactions. Thus, the polarity of the surface relative to the solvent is critical for molecular adsorption. These findings showhow adsorption/desorption can be precisely and systematically tuned by appropriate choice of both solvent and surface, and contribute to a predictive strategy for the design of catalytic and separations processes.

Introduction

Modulating the polarity of the condensed phase environment by the choice of solvent is a promising strategy to improve the efficiency of emerging energy technologies like the valorization of biomass, by increasing the activity and selectivity of catalysts.[1–3] For example, the levulinic acid yield from acid-catalyzed dehydration of mono- and oligosaccharides is highest in water compared to THF or toluene, since oligomerization side-reactions are suppressed by better solvation of sugars and their dehydration products in the aqueous solution.[4] The polarity of an reaction medium can also be modified by including a co-solvent, or by adding a salt.[5,6]

In the case of heterogeneous catalysts, surface polarity can influence catalytic activity by altering the adsorption of molecules at or near the active sites, as well as the activation barriers for reactions at those sites. Thus, Pd nanoparticles supported on a hydrophilic zeolite showed higher furfural conversion and selectivity to furan compared to Pd on a hydrophobic zeolite, due to the higher affinity of the former catalyst support for the reactant relative to the product.[7] Although the surface polarity can be changed by modifying the chemical composition of the catalyst,[1,2,8] other influential characteristics such as textural properties, the extent of confinement, the number of active sites, and even their identity, can also change. The resulting complexity hinders the investigation of correlations between surface polarity and catalytic activity/selectivity. For example, the surface polarities of zeolites and ZrO_2 increase in parallel with increasing numbers of strong Brønsted acid sites.[9,10] To achieve a desired reactivity, it is necessary to be able to tune the polarity of both the catalyst and the solvent system precisely *and independently*.

Some catalyst support materials, such as silicas and carbons, are readily modified post-synthesis with varying types and concentrations of chemically distinct components that alter the surface polarity.[7,11,12] For example, the pore surfaces of periodically-ordered mesoporous silicas (e.g., MCM-41, SBA-15) can be functionalized by anchoring hydrocarbon chains and/or other functional groups to change the interfacial polarity.[13,14] However, other synthesis methods do not allow independent control of polarity and textural properties.[7,14,15] Co-condensation is a powerful strategy to separate these effects, since two or more different types of (organo)silane precursors can be incorporated in varying amounts, while controlling the morphology through the use of a templating agent.[16] Nevertheless, differences in condensation rates can cause significant changes in surface area and/or pore volume, and

[a] *Department of Chemical Engineering, University of California, Santa Barbara, California 93106-5080, United States. E-mail: songihan@ucsb.edu; sscott@ucsb.edu*
[b] *Department of Chemistry & Biochemistry, University of California, Santa Barbara, California 93106-9510, United States*
† Electronic Supplementary Information (ESI) available: See DOI: 10.1039/x0xx00000x

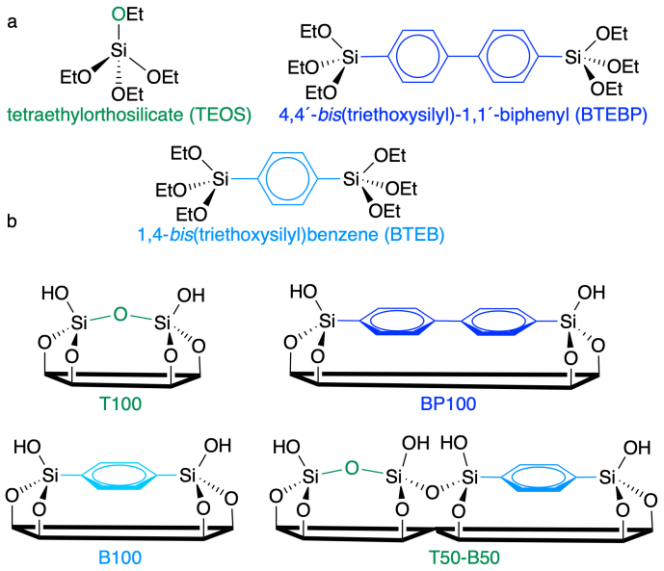

Scheme 1 (a) Chemical structures of the three silica precursors used in this work, and (b) the surface compositions of some of the resulting SBA-15-type materials.

increase variability in the series of target materials.[17,18] In addition, the spatial distribution of the co-condensed organosilanes may be non-random.[19]

In this work, we synthesized a family of periodic mesoporous organosilicas (PMOs) with similar meso- and macrostructures, surface areas and pore volumes, by co-condensing an inorganic silica source with varying amounts of two organodisilanes to create hybrid SBA-15-type materials with gradually increasing organic content (Scheme 1).

A method of assessing surface polarity is required to relate the effect of compositional changes to adsorption. Contact-angle measurements and water vapor adsorption isotherms correlate with surface polarity,[7,20,21] but their interpretation is complicated for rough surfaces and porous materials. Instead, we determined the polarity of each PMO by comparing the fluorescence of an adsorbed solvatochromic dye, Prodan, with the fluorescence of the same dye in various solvents of known polarity. This technique was used in a previous study to estimate the interfacial polarity of MCM-41-type materials whose pore surfaces were functionalized with diverse organic groups such as methoxypropyl, cyanoethyl, etc.[13] In addition, we used EPR lineshape analysis to assess changes in mobility of TEMPO (2,2,6,6,-tetramethylpiperidinyloxy) spin labels covalently attached to and interacting with PMO surfaces.[22,23] Finally, we explored how surface and solvent polarity together control the extent of adsorption of representative organic molecules relevant to the upgrading of lignocellulosic biomass.

Experimental section

Chemicals

Tetraethylorthosilicate (TEOS, 98%), 1,4-bis(triethoxysilyl)benzene (BTEB, 96%), 4,4'-bis(triethoxysilyl)1-1'-biphenyl (BTEBP, 95%), Pluronic 123, *p*-cresol (99%), phenol (99%), furfural (99%), anisole (>99%), vanadium oxytrichloride (99%), *N*-(3-dimethylaminopropyl)-*N*-ethylcarbodiimide hydrochloride, and *N,N*-dimethyl-6-propionyl-2-naphthylamine (Prodan) were purchased from Sigma Aldrich. 4-Carboxy-TEMPO and 3-aminopropyldimethylethoxysilane were purchased from Santa Cruz Biotechnology and Gelest, Inc., respectively. Deuterium oxide (99.9%), dimethylsulfoxide-d_6 (99.9%) and benzene-d_6 (99.5%) were obtained from Cambridge Isotope Laboratories, Inc. All chemicals were used as-received.

Synthesis of PMOs based on TEOS, BTEB, and their mixtures (i.e., T100, B100, and intermediate compositions)

To ensure a homologous series of porous materials with similar textural properties, we prepared all materials in-house, by adapting a literature procedure for the synthesis of SBA-15.[24] Pluronic P123 (3.0 g) was dissolved with a stirring in 0.2 M aqueous HCl (106 mL) overnight in a tightly sealed glass flask. The solution temperature was lowered to ~2 °C with an ice bath and TEOS (30 mmol, 6.68 mL) was added dropwise at a rate of ca. 1 mL/min while stirring at 150 rpm. After 1 h, the solution was heated to 40 °C in a water bath and stirred for 23 h. The reaction mixture was transferred to a Parr pressure reactor equipped with a Teflon liner (125 mL). After heating in an oven at 100 °C for 48 h, the resulting suspension was filtered and washed with ~500 mL water, then dried overnight in air at 100 °C. Residual P123 was removed by ethanol Soxhlet extraction at 110 °C in an oil bath for 24 h. Finally, the material was dried at 70 °C in air for 12 h to remove ethanol and the remaining P123 was eliminated by calcination at 250 °C in air for 3 h. At this temperature, P123 decomposes but organic groups in the framework are preserved (Fig. S1).[25]

The synthesis procedure was adjusted to prepare the material based on BTEB. In general, fully siliceous SBA-15 is most readily synthesized under acidic conditions, with HCl concentrations in the range 1.5-2.0 M (corresponding to a HCl:H_2O molar ratio of ca. 0.03). However, when BTEB was injected in this pH range, the hydrothermal reaction at 40 °C for 24 h gave a dense white precipitate and a semi-transparent gel. Since the hydrolysis of the organodisilane is much faster than that of TEOS,[26–28] the organosilane condensed rapidly without sufficient interaction with P123, resulting in a poorly ordered structure. The XRD pattern of the powder recovered from the white precipitate lacks the (110) and (220) reflections characteristic of long-range mesopore ordering. A lower HCl:H_2O molar ratio (between 10^{-3} and 10^{-4}) is known to retard the hydrolysis/condensation of the organosilane, although mesoscale ordering is not greatly affected until the isoelectric point (pH ~2) is reached.[27,28] Therefore a ten-fold smaller HCl concentration, 0.2 M, was used to prepare the phenylene-bridged organosilica material.

PMOs containing various fractions of phenylene bridging groups in the framework were synthesized using mixtures of TEOS and BTEB, adjusting the relative amounts of the precursors as shown in Table S1 to ensure mesostructure formation. The appropriate ratio is determined by the strengths of the interactions of each silane with P123. Each material is named according to the type of silane precursor (T: TEOS; B:

BTEB; BP: BTEBP) and their relative proportions. For example, T50-B50 was synthesized using 50 mol% TEOS and 50 mol% BTEB as silica precursors.

Synthesis of BTEBP-containing PMOs

Well-ordered B75-BP25 was made following the procedure described above, by co-condensing 5.5 mmol BTEB with 1.8 mmol BTEBP. However, the same reaction conditions did not lead to mesophase formation in the fully biphenylene-bridged PMO (BP100). Therefore, BP100 was synthesized using 1-butanol[29,30] as a co-surfactant with P123, following the method described by Yang et al.[31] First, the P123 was dissolved in acidic aqueous solution (0.5 M HCl, 106 mL), then 1-butanol (11 mmol) was added at room temperature. After stirring for 1 h, BTEBP (6.5 mmol) was added and the solution temperature was increased to 40 °C. After 24 h, the reaction mixture was transferred to a Parr pressure reactor (125 mL), where it was aged at 100 °C for 48 h. The surfactant was removed following the procedure described above.

Materials characterization

Powder X-ray diffraction patterns were acquired from 0.5 to 3.0° [2θ], and from 5 to 40° [2θ], using a Rigaku X-ray diffractometer equipped with Cu Kα radiation. N_2 sorption isotherms were measured at 77 K using 3Flex Micrometrics equipment. Before measurement, each material was outgassed at 423 K for 8 h in flowing N_2 to remove physically adsorbed water. The apparent surface area was calculated using the Brunauer-Emmett-Teller (B.E.T.) equation, assuming a molecular area for adsorbed N_2 of 0.135 nm^2.[32] The total pore volume was obtained from the amount of N_2 adsorbed at P/P_0 = 0.99. The average pore diameter was calculated by analyzing the adsorption branch of the N_2 isotherm, using the Barret-Joyner-Halenda (B.J.H.) method. ^{13}C CP-MAS NMR spectra were acquired at room temperature on a 500 MHz WB Bruker Avance NMR Spectrometer, in an 11.7 T magnetic field. Thermal gravimetric analysis of PMOs was performed with TA Discovery Thermo-Gravimetric Analyzer in the temperature ranging from 50 to 720 °C (under air, 10 °C/min).

Silanol group quantification

The number of accessible surface silanol groups was determined via their reaction with $VOCl_3$.[33] A PMO sample (ca. 40 mg) was placed in a Schlenk flask and evacuated at 0.1 mTorr and 170 °C for 7 h to remove physisorbed water. Its absence from the dry PMO was confirmed by IR. Excess $VOCl_3$ vapor (ca. 1 mmol) was transferred under reduced pressure at room temperature and allowed to react for 30 min. The chemisorbed vanadium was extracted from a precisely weighed sample (approx. 10 mg) by stirring in 5 mL of 1 M H_2SO_4 solution containing H_2O_2 (0.26 M).[33] The resulting solution contains a mixture of red-brown *mono*- and *bis*(peroxo)vanadium(V) complexes. The absorbance, measured at 448 nm using a Shimadzu UV-2401 UV-vis spectrophotometer, was compared to a calibration curve prepared using ammonium vanadate under same experimental conditions. The calculation of vanadium content was corrected for the change in PMO mass caused by modification with $VOCl_3$ as follows: for x mg V-modified PMO, and a measured vanadium concentration in the solution of y mmol/mL, the amount z of unmodified PMO present in the analysis solution (mg/mL) is $z = (x/5) - 136.8y$, where 136.8 mg/mmol is the difference in molecular between [$VOCl_2$] and the proton it replaces. Since the vanadium content is equal to the number of accessible silanols,[33] the SiOH surface density (α_{OH}) is y/z mmol/mg.

Fluorescence measurements

An aqueous solution of Prodan (15 μM) was prepared by vigorous stirring at room temperature for 6 h. Each PMO (20 mg) was stirred with 15 mL Prodan solution for 10 h, then centrifuged at 3000 rpm for 15 min. The supernatant liquid was decanted and the solid was dried at 100 °C for 6 h in air. Emission spectra for the dry powders were recorded with a Horiba FluoroMax 4 spectrometer, using an excitation wavelength of 365 nm. The peak maximum λ_{max} was identified as the zero-crossing of the first-derivative. Spectra were also acquired for each PMO powder dispersed in water. For both types of measurement, relative polarity values were interpolated using the solvent correlation between relative polarity[34] and the λ_{max} reported for dissolved Prodan,[35] fitted using a second-order polynomial function.

EPR spectroscopy

For selected PMOs, a small fraction (ca. 1 %) of surface silanols were modified with TEMPO (the spin label), using the coupling reaction between tethered propylamine and carboxy-substituted TEMPO, following a slightly modified literature procedure.[36,37] Each PMO (20 mg) was suspended in phosphate buffered saline solution (pH 7.4, 2 mL), then 3-aminopropyldimethylethoxysilane (APDMES, 16 μL) was added and the mixture was stirred for 18 h at room temperature. The solid was separated by centrifugation and combined with 4-carboxy-TEMPO (0.5 mL, 10 mM in 2-morpholin-4-ylethanesulfonic (MES) acid buffer, pH 4.5) and *N*-(3-dimethylaminopropyl)-*N*-ethylcarbodiimide hydrochloride (1.2 mL, 50 mM in pH 4.5 MES buffer).

After 48 h incubation at room temperature, the mixture was centrifuged at 3000 rpm for 4 min. (Previously, a much shorter reaction time, 30 min, was reported for TEMPO functionalization of amine-modified non-porous silicas.[37] Here, this procedure led to partial peptide bond cleavage, possibly catalyzed by residual unreacted propylamine groups during the subsequent EPR measurement. Extending the reaction time prevented contamination of the EPR spectra by contributions from untethered radicals.) The supernatant liquid was removed and the solid was resuspended in DI water. This step was repeated 10 times to ensure complete removal of unreacted 4-carboxy-TEMPO, as judged by the absence of EPR signals for the untethered radical. No signals for untethered radicals reappeared for the duration of the EPR measurement (ca. 6 h). The spin-labeled material (ca. 4 μL of a PMO slurry, 40 mg/mL) was placed in a quartz capillary (0.60 mm I.D., 0.84 mm O.D.).

X-band continuous-wave (CW) EPR spectra were recorded on a Bruker EMSplus EPR spectrometer, using a Bruker ER 4119HS-LC high sensitivity resonator at a microwave frequency of ca. 9.3 GHz, with 1 mW irradiation power and 0.4 G modulation width. The spectra were simulated by lineshape fitting using the SimLabel software,[38] which relies on the same functions as EasySpin.[39]

Quantitative adsorption measurements

Each PMO (20 mg) was mixed with a solution containing the desired amount of *p*-cresol, phenol, or furfural (dissolved in 1.5 mL of the specified deuterated solvent) in a 2 mL centrifuge tube. The slurry was agitated in an IKA Vortex 4 digital mixer at 3000 rpm for 10 h, then centrifuged at 3000 rpm for 8 min to separate the solid. The decanted supernatant was analyzed by solution-state ^{1}H NMR (Varian Unity, 500 MHz), using DMSO as an internal standard. When organic molecules were adsorbed directly from DMSO-d_6, the residual solvent peak was used as the standard instead.

Results and discussion

Synthesis and Characterization of Periodic Mesoporous Organosilicas (PMOs)

In order to obtain materials with uniform morphologies and a range of surface polarities, a series of SBA-15-type PMOs were synthesized. As (organo)silica precursors, three different silanes: tetraethylorthosilicate (TEOS), 1,4-bis(triethoxysilyl)benzene (BTEB), and 4,4´-bis(triethoxysilyl)-1,1´-biphenyl (BTEBP), were chosen for incorporation in various ratios into the ordered mesoporous SBA-15 framework (Scheme 1a). The fully inorganic TEOS-based material (T100) is expected to have the most polar surface, while the BTEBP-based PMO (BP100) should be the least polar due to its bridging biphenylene groups, Scheme 1b. Intermediate surface polarities are expected for the BTEB-based material (B100), and for co-condensed mixtures of TEOS/BTEB, or BTEB/BTEBP.

Representative SEM images for the PMOs show elongated fibers with diameters of 0.3-0.6 µm and lengths of 2-10 µm (Fig. S2), consistent with previous studies.[24,25] However, BP100 has a distinctive, particulate structure. The incorporation of phenylene and/or biphenylene-bridged groups into the organosilica framework was confirmed by ^{13}C solid-state CP/MAS NMR (Fig. S3). Low- and wide-angle XRD patterns for the various PMOs were recorded after surfactant removal (Figs. S4 and S5). The appearance of clear d_{110} and d_{220} reflections in the low-angle region is evidence for mesopores with a high degree of long-range order for all materials except BP100. The positions of the d_{100} reflections are similar, although the peak position for T100 indicates a slightly larger unit-cell size (from ca. 120 to 130 Å). Assuming similar wall thicknesses, this material has a slightly larger pore size. The XRD pattern of BP100, whose synthesis requires the use of a 1-butanol as co-surfactant to ensure mesophase formation, does not contain clear low-angle peaks, implying less uniform pores. Its pore size distribution was obtained by N_2 physisorption, and showed a broad distribution (Table 1, Fig. S6a).

Table 1 Physicochemical properties of PMO materials

PMO	B.E.T. surface area [a] (m^2/g)	pore volume [b] (cm^3/g)	pore size [c] (nm)	Silanol surface density, α_{OH} (mmol/g) [d]	(OH/nm^2) [e]
T100	709	1.12	9.7 ± 0.5	2.1	1.8
T75-B25	668	0.99	7.6 ± 0.3	1.7	1.5
T50-B50	694	1.00	7.5 ± 0.7	1.7	1.5
T25-B75	708	1.08	7.1 ± 0.7	2.1	1.8
B100	721	1.08	7.7 ± 0.8	1.5	1.3
B75-BP25	719	1.01	6.3 ± 0.3	2.1	1.8
BP100	728	1.52	5.0 ± 3.6	1.9	1.6

[a] Calculated using the Brunauer-Emmett-Teller (B.E.T.) method. The generally accepted measurement error in B.E.T. surface areas is ± 10 %.[40] The calculations assume an area for adsorbed N_2 of 0.135 nm^2/molecule, which is the value appropriate for perpendicular adsorption on oxide surfaces.[32] Since N_2 adsorbs parallel to the surface on organic materials, occupying a larger area (0.162 nm^2), the actual surface areas of the organosilicas may be somewhat higher, but the fractions of parallel vs. perpendicularly adsorbed N_2 are not known. Finally, B.E.T surface areas normalized by mass do not reflect differences in skeletal densities for silicas with different organic fractions. [b] measured at P/P_0 = 0.99. [c] Calculated using the Barrett-Joyner-Halenda (B.J.H.) method, using the adsorption branch of the isotherm, and reported as the average pore size. [d] The measurement error associated with these values is estimated to be ± 0.1 mmol/g. [e] The error generated due to the experimental uncertainty in the surface area measurements is ± 0.3 nm^{-2}.

The physicochemical properties of all PMOs are compared in Table 1. Their B.E.T. surface areas vary over a relatively small range, from 668 to 728 m^2/g, as do their B.J.H. pore sizes (6.3 to 7.7 nm) and pore volumes (0.99 to 1.12 cm^3/g). The slightly higher pore size for T100 (9.7 nm) is consistent with its lower angle d_{100} peak position, while the increased pore volume for BP100 (1.52 cm^3/g) is attributed to the interparticle porosity as confirmed by the N_2 adsorption isotherm (Fig. S6b).[31] Nevertheless, the variability is small compared to materials used in previous comparative studies of surface polarity effects on catalysis (for which reported surface areas, pore sizes or pore volumes varied by factors of 2-4).[9,15,41] Thus, the PMOs used in this work are well-suited for isolating the effect of surface polarity on adsorption capacity, while keeping structural factors constant.

Surface hydroxyl content

Condensation of TEOS and/or organodisilanes followed by hydrolysis creates pore surfaces terminated with hydroxyl groups, some of which resist condensation even at very high temperatures.[42] Surface polarity is affected by the surface density of these silanols, as well as by the nature and extent of organic content at the interface. The surface silanols present in each PMO were quantified by their reaction with $VOCl_3$.[33] The number of $VOCl_3$-accessible surface OH groups is fairly constant, ranging from 1.5 to 2.1 mmol/g (1.3-1.8 OH/nm^2, Table 1). However, these surface silanol contents are 2-3 times smaller than previously reported values for SBA-15 (3.5 mmol/g)[43] and MCM-41 (3.6 to 5.3 mmol/g).[43,44] We note that conventional

measurement methods count both accessible surface OH groups and inaccessible sub-surface OH groups. A study of the number of such sites that react with trimethylsilyl chloride reported much lower OH contents for SBA-15 and MCM-41 (1.8 and 2.2 mmol/g, respectively).[43] These values are closer to the number of surface OH groups measured here. Thus, SBA-15-type materials synthesized using TEOS, BTEB, and BTEBP precursors have similar numbers of accessible silanol groups, and differ significantly only in the type and amount of framework organic groups.

Solvatochromic Assessment of Surface Polarity

Water affinity (i.e., hydrophilicity) is related indirectly to surface polarity.[7,45] For example, water vapor adsorption isotherms were used to obtain qualitative information about the surface wettability of microporous carbons and mesoporous silicas, via comparison of the onset pressures for pore condensation.[20,21] However, hydrophilicity and polarity are distinct physical properties. Polarity can be probed more directly using an organic dye such as Prodan, whose electronic energy levels are affected by non-covalent interactions with its surroundings. The wavelength of maximum fluorescence intensity for Prodan depends on the polarity of the solvent in which the dye is dissolved (Fig. 1a). Increasing solvent polarity is associated with a gradual shift in the emission spectrum.[11,13,35]

Thus adsorbed Prodan can report on changes in the polarity of PMO surfaces due the presence of surface organic groups. Fig. 1b shows the range of emission colors for Prodan adsorbed on three representative PMO powders, each Emission spectra for Prodan adsorbed on the various dry PMO powders are shown in Fig. 2a. The shortest fluorescence emission wavelength, for BP100 (λ_{max} 473 nm), is consistent with its lower polarity compared to B100 (λ_{max} 489 nm) and T100 (λ_{max} 509 nm, Table S2). The gradual shift of λ_{max} for intermediate PMO compositions shows that the surface polarity of these materials can be precisely tuned.

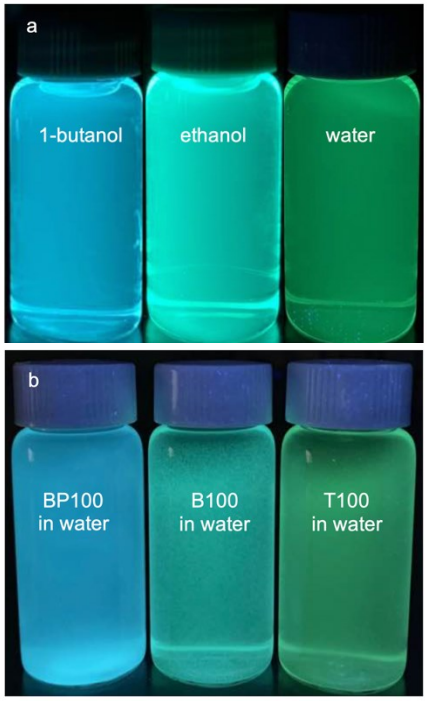

Fig. 1 Comparison of Prodan fluorescence: (a) dissolved in the various solvents indicated; and (b) adsorbed on three different PMO materials, all suspended in water.

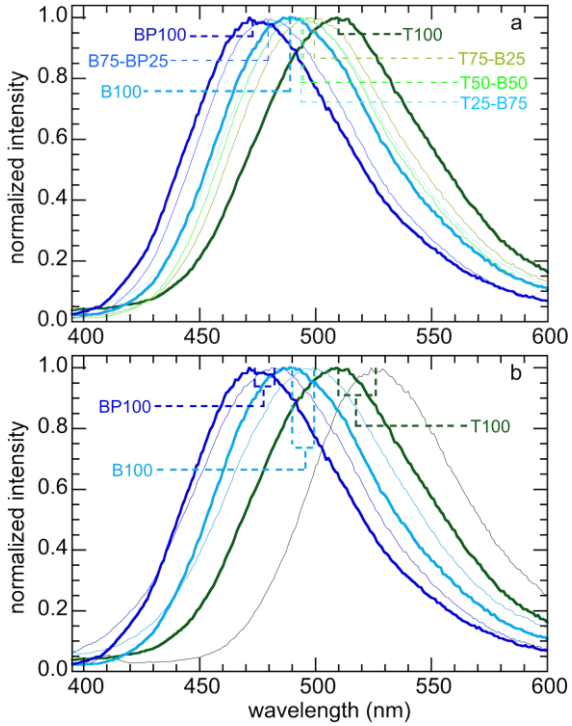

Fig. 2 Normalized emission spectra of Prodan: (a) adsorbed on various dry (organo)silica powders; and (b) comparison of selected dry powders (heavier lines) with the same powders suspended in water (lighter lines).

Fluorescence spectra were also recorded for aqueous suspensions of each PMO, following a previously described method.[11,13] Fig. 2b compares the spectra for selected materials with those for Prodan adsorbed on the corresponding dry powders. Dispersion of a PMO in water results in a red-shift in the corresponding emission spectrum, consistent with greater surface hydration and hence increased interfacial polarity. However, the magnitude of the shift in λ_{max} is not constant. It is largest (17 nm) for the most polar material, T100, and smallest (9 nm) for the least polar material (BP100). Thus the extent of hydration is therefore higher for the more polar surfaces. This phenomenon, while expected, has implications for adsorption of solutes from aqueous solutions (see below).

Relative surface polarity values for each PMO were obtained using λ_{max} values for the adsorbed Prodan and interpolating λ_{max} values measured in various solvents of known polarity (Table S3).[35] The results are shown for both dry and wet PMO materials in Fig. 3 and Table S4. The dry PMO powders have *relative surface polarities* ranging from 0.50 to 0.81. Surface hydration causes all values to increase when the powders are suspended in water. The relative polarity of dry T100 is similar to that of methanol, while hydrated T100 has a polarity close to that of water. Dry BP100 is less polar than 1-octanol, but wet BP100 has a surface polarity closer to that of 1-butanol. The relationship

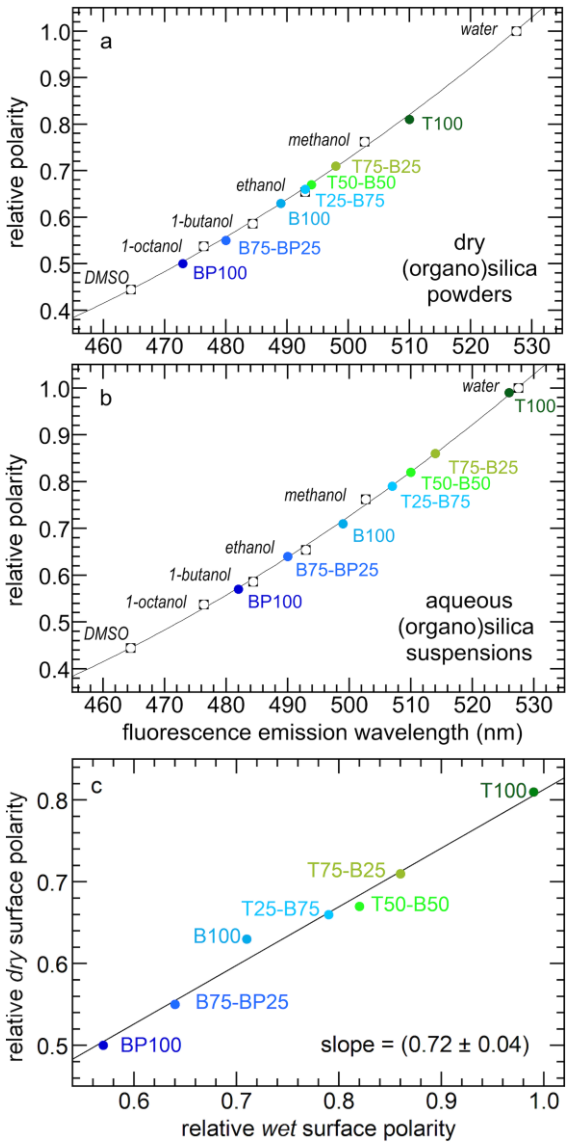

Fig. 3 Correlations between the relative polarities of various solvents[34] and Prodan fluorescence emission maxima for (a) dry PMO powders, or (b) PMOs suspended in water; and (c) relationship between the relative surface polarities of the dry PMO powders and their aqueous suspensions.

between pairs of λ_{max} values is linear, although the slope is not unity (Fig. 3c).

Mobility of Adsorbed Species

Molecular mobility is inversely correlated with adsorption strength. EPR line-shape analysis provides information about the relative mobility of surface-confined spin labels.[46–48] We acquired EPR spectra of dilute TEMPO radicals attached to aminopropylsilane-modified PMOs (Scheme S1). Low spin concentrations minimize EPR line-broadening effects caused by strong dipolar interactions between neighboring spin labels,[46] therefore only a small fraction (ca. 1 %) of surface silanols were functionalized with the nitroxide radicals. X-band EPR spectra recorded at room temperature for the spin-labeled PMOs suspended in water are shown in Fig. 4. Variations reflect differences in the average local dynamics of the tethered spin-

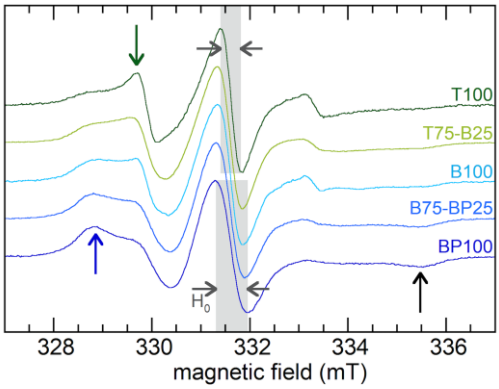

Fig. 4 Continuous-wave EPR spectra, recorded at room temperature, for various 4-carboxy-TEMPO-functionalized PMOs suspended in water. Blue and green arrows indicate peaks associated with slower- and faster-moving radicals, respectively. The emergence of a weak peak at high field (black arrow) is also characteristic of an increased fraction of slow-moving radicals.

labeled moieties due to the strength of their interactions with the surface, Scheme 2.

Restricted spin motion caused by greater proximity of the tethered radical to the surface results in incomplete averaging of anisotropic terms of the magnetic Hamiltonian. This effect is manifested qualitatively in various types of line broadening and appearance of distinct spectral features.[49,50] First, the line width (H_0) of the central peak increases gradually,[22,51] from 0.47 to 0.67 mT (grey-shaded region) with decreasing surface polarity from T100 to BP100. The eventual appearance of an outer extremum at 335.5 mT (black arrow) is also a well-established indicator of diminished rotational motion.[22,50] In addition, the gradually changing intensities of two partially resolved peaks at 328.8 mT (blue arrow) and 329.7 mT (green arrow) represent varying populations of slow and fast components, respectively. Further line broadening is caused by the increasing fraction of the slow component.

The A_{zz} component of the nitrogen hyperfine tensor element parallel to B_0 (i.e., aligned with the *z*-direction) also varies with local polarity, due to changes in localization of the unpaired electron along the N-O bond axis (perpendicular to the

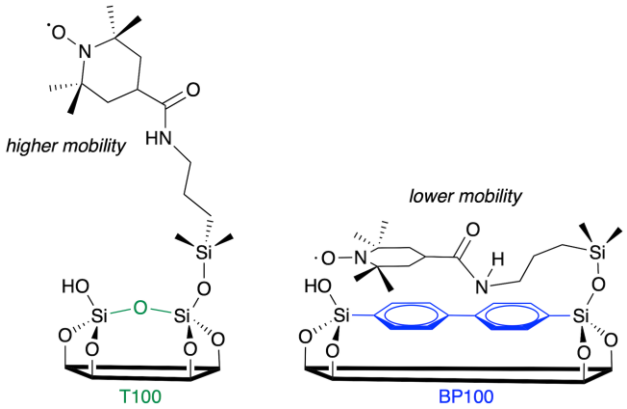

Scheme 2 Two possible orientations of tethered TEMPO spin labels, with different mobilities depending on the extent of their interaction with the PMO surface.

Table 2 Characteristics of deconvoluted EPR spectra of TEMPO-modified PMOs

Material	A_{zz} (mT)[a]	τ_D (ns)[b]	
		Faster	Slower
T100	3.93	2.6 (0.61)	7.1 (0.39)
B100	3.83	3.3 (0.31)	7.4 (0.69)
BP100	3.76	3.5 (0.14)	8.6 (0.86)

[a] Measured at 120 K. [b] Values in parentheses represent fractional contributions for each component at room temperature.

z-axis) modulated by changes in the local electric field.[23] In spin-labeled membrane proteins, A_{zz} values were reported to increase from 3.43 to 3.65 mT with increasing polarity of the membrane and the protein micro-environment.[23] X-band EPR spectra of suspensions of BP100, B100 and T100, acquired at 120 K, are shown in Fig. S7. They also show that A_{zz} increases gradually with increasing polarity, from 3.76 to 3.93 mT (Table 2).

In order to quantify changes in the relative mobilities of tethered TEMPO radicals, the room temperature EPR spectra of T100, B100 and BP100 were deconvoluted into two components. These components represent faster- and slower-moving populations of the spin label, corresponding to radicals experiencing weaker and stronger interactions, respectively, with the PMO surface. Simulations were performed with the appropriate A_{zz} value for each PMO (measured at low temperature) and a reported value of the *g*-tensor of the TEMPO radical[52] (precise determination of the *g*-tensor would require lineshape analysis at higher field.)[53] The simulated EPR spectra and their deconvoluted components are shown in Fig. 5.

For the most polar material (T100), the correlation times (τ_D) for the faster- and slower-moving components are 2.6 and 7.1 ns, respectively, with fractional contributions of 61 and 39 % (Table 2). For the least polar material (BP100), both correlation times are higher (3.5 and 8.6 ns), as is the fractional contribution of the slower component (86 %). These changes are consistent with stronger interactions (and therefore lower mobility) with the less polar surface for a higher fraction of the tethered spin labels.

Effect of surface polarity on molecular partitioning at solid-liquid interfaces

Three different molecules (phenol, *p*-cresol, furfural) considered representative of common types of functional groups present in lignocellulosic biomass were adsorbed on PMOs across the full range of surface polarities. Fig. 6a shows the adsorption isotherms for three PMOs (T100, B100, and BP100) in contact with aqueous phenol solutions (with initial phenol concentrations from 10 to 85 mM) at 296 K. Although phenol can interact with the surface hydroxyl groups of silica via hydrogen-bonding, its affinity for hydrated T100 is very low. Furthermore, even though all three silicas have similar surface hydroxyl densities (Table 1), the extent of phenol adsorption increases dramatically as the surface becomes less polar. Thus, phenol is much more strongly adsorbed onto B100 and BP100 (maximum values of ca. 0.7 and 1.3 mmol/g, respectively).

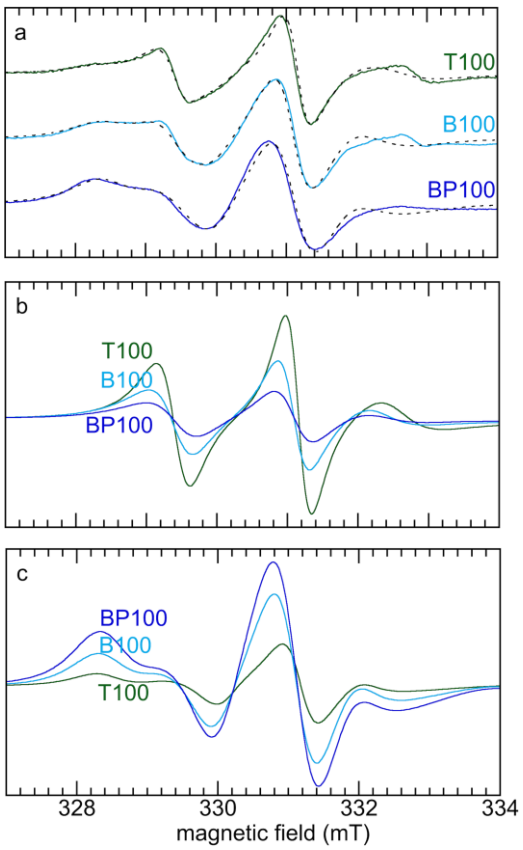

Fig. 5 (a) Comparison of experimental (solid color lines) and simulated (dashed black lines) EPR spectra for three PMOs functionalized with TEMPO, and deconvolution of each EPR spectrum into (b) faster, and (c) slower components. Simulations were performed using g = [2.0097, 2.0064, 2.0025],[52] and measured A_{zz} values (Table 2). Values for A_{xx} and A_{yy} (0.7 and 0.8 mT, respectively) were obtained as global curvefit parameters. The fraction of each component and its correlation time were refined for each fit.

The adsorption isotherms for B100 and BP100 were analyzed with the Langmuir model, assuming monolayer sites. Eq 1 relates *q* (the uptake of the adsorbate, in mmol/g adsorbent) to C_e (the equilibrium concentration in solution). Q_L

$$q = \frac{Q_L K_L C_e}{1 + K_L C_e} \quad (1)$$

is the maximum adsorption capacity, and the Langmuir constant K_L represents the affinity of the adsorption sites for the adsorbate. Non-linear curvefit parameters are shown in Table 3. The larger values of Q_L and K_L for BP100, compared to B100, confirm that phenol has a higher affinity for the biphenylene-containing surface relative to the phenylene-containing surface. For neutral adsorbates, or adsorbates with small charges, K_L is essentially equal to the thermodynamic equilibrium constant $K°$.[54] The temperature dependence of $K°$ is described by the Van't Hoff equation (eq 2). The enthalpy of phenol adsorption,

$$ln\, K° = \Delta S°/R - \Delta H°/RT \quad (2)$$

$\Delta H°$, was obtained by extracting K_L from adsorption isotherms recorded at different temperatures (Fig. 6b). According to Fig. 6c, the value of $\Delta H°$ for phenol adsorption from water onto BP100 is -(5.8 ± 3.2) kJ/mol, similar to a previously reported value for bentonite clay with intercalated

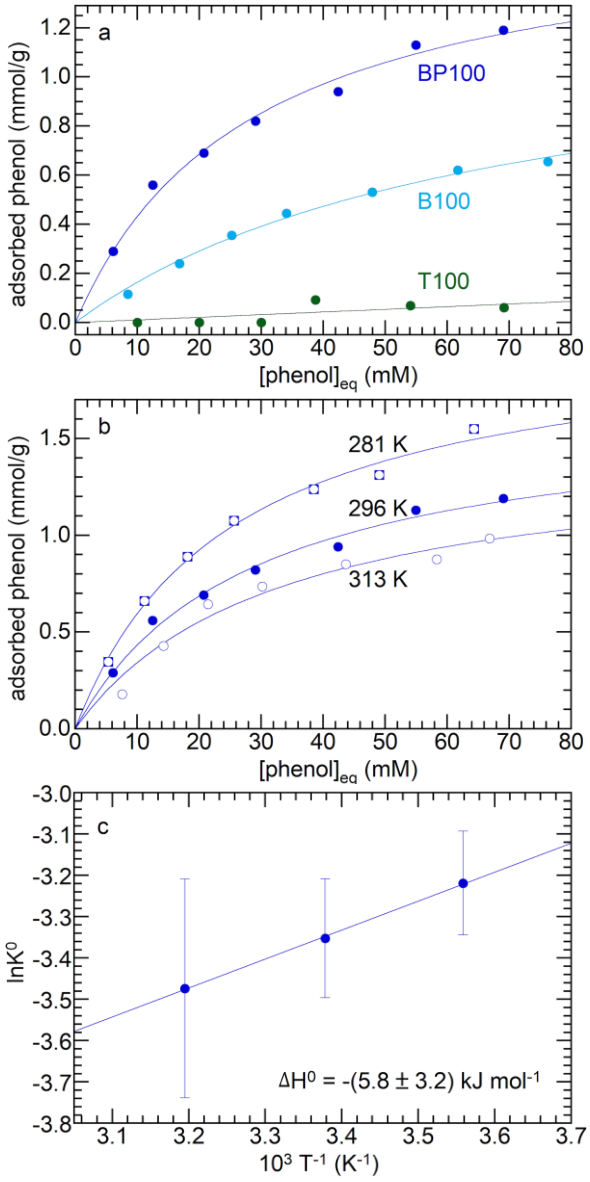

Fig. 6 Adsorption of phenol from water, onto: (a) T100, B100 and BP100, all at 296 K, and (b) BP100 at 281, 296, and 313 K. The isotherms (solid lines) represent non-linear curvefits using the Langmuir model (eq 1). (c) Van't Hoff plot for determination of adsorption enthalpy.

hexadecyltrimethylammonium ions (-10.4 kJ/mol).[55] The small values arise because they represent the difference between the much larger enthalpies of phenol and water adsorption, and include the effect of phenol desolvation.[56]

To investigate how systematically changing the surface polarity affects molecular adsorption, the phenol affinities of the entire PMO series were measured. Adsorption is suppressed

Table 3 Langmuir analyses[a] of phenol adsorption from water onto PMOs

Material	T (K)	Q_L (mmol/g)	K_L (L/mmol)
B100	296	1.26 ± 0.11	0.015 ± 0.002
BP100	313	1.45 ± 0.17	0.031 ± 0.008
	296	1.66 ± 0.10	0.035 ± 0.005
	281	2.07 ± 0.10	0.040 ± 0.005

[a] Based on non-linear curvefits of the data presented in Fig. 6, using eq 2.

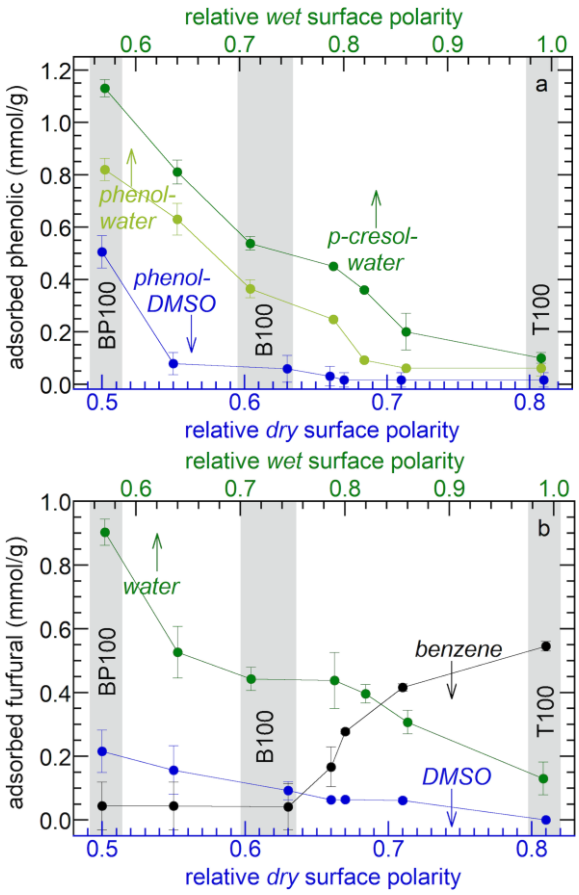

Fig. 7 Effect of PMO polarity on (a) amounts of phenol or *p*-cresol adsorbed from 40 mM solutions in water and DMSO; and (b) amounts of furfural adsorbed from 40 mM solutions in various solvents. In each experiment, 20 mg PMO was combined with 1.5 mL solution at 296 K.

on more polar surfaces, which are more strongly hydrated (see above). Therefore aqueous solutions of phenol show monotonically decreasing adsorption as the polarity of the PMO increases (Fig. 7a, Table S5). Formulated in terms of a Born-Haber cycle, the heat of adsorption represents the enthalpy costs to disrupt water-surface and water-phenol interactions, as well as the enthalpy gained in new water-water and phenol-surface interactions.[56] The water-phenol and water-water contributions are the same for all materials, therefore the higher phenol affinities of the less polar PMOs result from a combination of weaker water-surface interactions (as shown in Fig. 3c above) as well as stronger phenol-surface interactions. Other interactions unique to surface aromatic groups (phenylene and biphenylene), such as H-π and π–π interactions, may also contribute to the higher phenol affinities of the less polar PMOs.[57]

The importance of solute-surface interaction contribution is evidenced by comparing the adsorption of the slightly less polar *p*-cresol (relative polarity 0.697) compared to phenol (relative polarity 0.701).[34] The effect of surface polarity on *p*-cresol affinity is even more pronounced (Fig. 7a). Thus B100 and BP100 adsorb 48 and 38 % more *p*-cresol, respectively, than phenol. Since the water-surface interactions are the same for both

solutes, these differences are attributed to stronger solute-surface interactions.

Effect of solvent polarity on molecular partitioning at the solid-liquid interface

The choice of the solvent modulates the effect of surface polarity on molecular adsorption. For example, the phenol affinities of all the PMOs are dramatically lower when DMSO is the solvent instead of water, Fig. 7a. Thus phenol adsorption onto B100 from a DMSO solution decreased by 87 %, compared to adsorption from an aqueous solution. Reasoning again in terms of Born-Haber cycles,[56] we first note that phenol-surface interactions do not depend on solvent choice. The enthalpy cost to disrupt DMSO-phenol interactions is expected to be higher than for water-phenol interactions, since the dielectric constant of phenol (12)[58] is closer to that of DMSO (46) than water (77, all at 30 °C).[59] In addition, the enthalpy cost for disrupting interactions of the solvent with the B100 surface is higher for DMSO than for water. Finally, solvent-solvent interactions are stronger for water than for DMSO. All three terms are expected to suppress adsorption of phenol from DMSO. Compared to B100, BP100 shows less suppression (38 %) of phenol adsorption upon changing the solvent from water to DMSO, presumably due to stronger phenol-surface interactions.

The effect of solvent polarity was further explored by comparing furfural adsorption from water, DMSO or benzene (with relative polarities of 1.00, 0.44, and 0.11, respectively). Similar to aqueous solutions of phenol and *p*-cresol, the furfural affinities of the PMOs from the polar solvent increase monotonically as the surface polarity decreases (Fig. 7b, Table S5). The same trend is observed in less polar DMSO, although the absolute amounts of adsorbed furfural are much lower (for the same reasons described above for phenol adsorption from DMSO). Since the polarity of furfural, as measured either by its dielectric constant (42)[60] or by the solvatochromic dye method (0.43),[60] is very close to that of DMSO, solvent and solute adsorption enthalpies are expected to be similar. In addition, solute-solvent interactions are presumably strong. The net result is a very weak effect of surface polarity on adsorption. However, the trend is dramatically reversed when furfural is dissolved in non-polar benzene. Now, the furfural affinities of the PMOs *decrease* with increasing surface polarity. Since benzene interacts weakly with furfural and with the more polar surfaces, furfural adsorption is favored. The three different trends in Fig. 7b succinctly illustrate the power of combining surface polarity modulation with an appropriate choice of solvent to tune molecular adsorption.

Conclusions

This study sets the stage for design of porous solid catalysts in conjunction with rational solvent choice to improve activity and selectivity in liquid-phase reactions by promoting preferential adsorption of reactants and desorption of desired products. The *relative surface polarities* of periodic mesoporous organosilicas (PMOs) can be tuned over a wide range by varying the chemical composition, independent of the textural properties. The mobility of near-surface molecules and their affinity for the surface are correlated with surface polarity. Tethered nitroxides experience decreased mobility as the surface polarity decreases, reflecting their increasingly strong association with the surface. Moreover, adsorption of organic molecules such as phenol, *p*-cresol, and furfural from polar solvents become *more* favorable as the surface polarity decreases. However, the effect can be reversed by changing the solvent polarity: thus such molecules adsorb *less* favorably from benzene as the surface polarity decreases. When the polarity of the solvent and solute are well-matched, adsorption is minimized. Thus, tuning the extent of adsorption precisely can be achieved by appropriate choices of solvent, surface polarity, *and* solute polarity.

This systematic study demonstrates how readily achieved variations in the surface polarity of PMO-based materials results in significant changes in adsorption equilibria for classes of molecules relevant to important catalytic reactions. While the consequences of surface and solvent polarity on adsorption are as expected, the ease with which the effects can be predicted and modulated suggests ways to design improved catalytic processes. Further refinements should include consideration of specific solute binding modes, such as cation-π interactions, electrostatic interactions, and H-bonding. Work is underway to include modification of PMO materials with active sites such as Brønsted/Lewis acid sites and metal nanoparticles, in order to assess polarity effects on heterogeneous reactivity.

Conflicts of interest

There are no conflicts to declare.

Acknowledgements

We are grateful to Jiafan Chen and Dr Jin-Ping Zhang (Suzhou Institute of Nano-Tech and Nano-Bionics) for some of the SEM images. We are grateful to Tarnuma Tabassum for her assistance with low temperature EPR measurements.We acknowledge funding from the U.S. National Science Foundation (NSF), Award No. CBET-1604095 (for materials synthesis and characterization) and CHE-1800596 (for surface spectroscopy). Some experiments made use of the MRL Shared Experimental Facilities, supported by the MRSEC Program of the NSF under Award No. DMR-1720256.

Notes and references

1 J. Manayil, A. Lee and K. Wilson, *Molecules*, 2019, **24**, 239.
2 F. Liu, K. Huang, A. Zheng, F.-S. Xiao and S. Dai, *ACS Catal.*, 2018, **8**, 372–391.
3 C. Sievers, Y. Noda, L. Qi, E. M. Albuquerque, R. M. Rioux and S. L. Scott, *ACS Catal.*, 2016, **6**, 8286–8307.
4 X. Hu, S. Wang, R. J. M. Westerhof, L. Wu, Y. Song, D. Dong and C.-Z. Li, *Fuel*, 2015, **141**, 56–63.
5 M. A. Mellmer, C. Sener, J. M. R. Gallo, J. S. Luterbacher, D. M. Alonso and J. A. Dumesic, *Angew. Chem. Int. Ed.*, 2014, **53**, 11872–11875.
6 M. J. Gilkey and B. Xu, *ACS Catal.*, 2016, **6**, 1420–1436.

7 C. Wang, Z. Liu, L. Wang, X. Dong, J. Zhang, G. Wang, S. Han, X. Meng, A. Zheng and F.-S. Xiao, *ACS Catal.*, 2018, **8**, 474–481.
8 P. A. Zapata, J. Faria, M. P. Ruiz, R. E. Jentoft and D. E. Resasco, *J. Am. Chem. Soc.*, 2012, **134**, 8570–8578.
9 R. Otomo, T. Yokoi and T. Tatsumi, *Appl. Catal., A*, 2015, **505**, 28–35.
10 L. Li, Y. Yoshinaga and T. Okuhara, *Phys. Chem. Chem. Phys.*, 1999, **1**, 4913–4918.
11 D. Singappuli-Arachchige, T. Kobayashi, Z. Wang, S. J. Burkhow, E. A. Smith, M. Pruski and I. I. Slowing, *ACS Catal.*, 2019, **9**, 5574–5582.
12 J. C. Manayil, V. C. dos Santos, F. C. Jentoft, M. Granollers Mesa, A. F. Lee and K. Wilson, *ChemCatChem*, 2017, **9**, 2231–2238.
13 D. Singappuli-Arachchige, J. S. Manzano, L. M. Sherman and I. I. Slowing, *ChemPhysChem*, 2016, **17**, 2982–2986.
14 B. Karimi and H. M. Mirzaei, *RSC Adv.*, 2013, **3**, 20655–20661.
15 B. Karimi, H. M. Mirzaei, H. Behzadnia and H. Vali, *ACS Appl. Mater. Interfaces*, 2015, **7**, 19050–19059.
16 C. Pirez, A. F. Lee, C. Jones and K. Wilson, *Catal. Today*, 2014, **234**, 167–173.
17 J. Liu, J. Yang, C. Li and Q. Yang, *J. Porous Mater.*, 2009, **16**, 273–281.
18 Y. Yang and A. Sayari, *Chem. Mater.*, 2008, **20**, 2980–2984.
19 T. Kobayashi and M. Pruski, *ACS Catal.*, 2019, **9**, 7238–7249.
20 R. H. Bradley and B. Rand, *Carbon*, 1993, **31**, 269–272.
21 J. B. Mietner, F. J. Brieler, Y. J. Lee and M. Fröba, *Angew. Chem. Int. Ed.*, 2017, **56**, 12348–12351.
22 J. P. Jahnke, M. N. Idso, S. Hussain, M. J. N. Junk, J. M. Fisher, D. D. Phan, S. Han and B. F. Chmelka, *J. Am. Chem. Soc.*, 2018, **140**, 3892–3906.
23 E. Bordignon, H. Brutlach, L. Urban, K. Hideg, A. Savitsky, A. Schnegg, P. Gast, M. Engelhard, E. J. J. Groenen, K. Möbius and H.-J. Steinhoff, *Appl. Magn. Reson.*, 2010, **37**, 391–403.
24 D. Zhao, J. Feng, Q. Huo, N. Melosh, G. H. Fredrickson, B. F. Chmelka and G. D. Stucky, *Science*, 1998, **279**, 548–552.
25 Y. Goto and S. Inagaki, *Chem. Commun.*, 2002, 2410–2411.
26 C. J. Brinker, *J. Non-Cryst. Solids*, 1988, **100**, 31–50.
27 X. Y. Bao, X. S. Zhao, S. Z. Qiao and S. K. Bhatia, *J. Phys. Chem. B*, 2004, **108**, 16441–16450.
28 X. Y. Bao, X. S. Zhao, X. Li, P. A. Chia and J. Li, *J. Phys. Chem. B*, 2004, **108**, 4684–4689.
29 F. Kleitz, L. A. Solovyov, G. M. Anilkumar, S. H. Choi and R. Ryoo, *Chem. Commun.*, 2004, 1536–1537.
30 T.-W. Kim, F. Kleitz, B. Paul and R. Ryoo, *J. Am. Chem. Soc.*, 2005, **127**, 7601–7610.
31 Y. Yang and A. Sayari, *Chem. Mater.*, 2007, **19**, 4117–4119.
32 L. Jelinek and E. sz. Kovats, *Langmuir*, 1994, **10**, 4225–4231.
33 G. L. Rice and S. L. Scott, *Langmuir*, 1997, **13**, 1545–1551.
34 C. Reichardt and T. Welton, *Solvents and solvent effects in organic chemistry*, 4th Ed., Wiley-VCH: Weinheim, 2011.
35 J. Catalan, P. Perez, J. Laynez and F. G. Blanco, *J. Fluoresc.*, 1991, **1**, 215–223.
36 J. H. Ortony, C.-Y. Cheng, J. M. Franck, R. Kausik, A. Pavlova, J. Hunt and S. Han, *New J. Phys.*, 2011, **13**, 015006.
37 A. M. Schrader, J. I. Monroe, R. Sheil, H. A. Dobbs, T. J. Keller, Y. Li, S. Jain, M. S. Shell, J. N. Israelachvili and S. Han, *Proc. Natl. Acad. Sci. U. S. A.*, 2018, **115**, 2890–2895.
38 E. Etienne, N. Le Breton, M. Martinho, E. Mileo and V. Belle, *Magn. Reson. Chem.*, 2017, **55**, 714–719.
39 S. Stoll and A. Schweiger, *J. Magn. Reson.*, 2006, **178**, 42–55.
40 A. Cubo, J. Iglesias, G. Morales, J. A. Melero, J. Moreno and R. Sánchez-Vázquez, *Appl. Catal., A*, 2017, **531**, 151–160.
41 K. Hammes, R. J. Smernik, J. O. Skjemstad and M. W. I. Schmidt, *J. Appl.*, 2008, **23**, 2113–2122.
42 L. T. Zhuravlev, *Colloids Surf., A*, 2000, **173**, 1–38.
43 M. Ide, M. El-Roz, E. De Canck, A. Vicente, T. Planckaert, T. Bogaerts, I. Van Driessche, F. Lynen, V. Van Speybroeck, F. Thybault-Starzyk and P. Van Der Voort, *Phys. Chem. Chem. Phys.*, 2013, **15**, 642–650.
44 J. P. Gallas, J. M. Goupil, A. Vimont, J. C. Lavalley, B. Gil, J. P. Gilson and O. Miserque, *Langmuir*, 2009, **25**, 5825–5834.
45 N. Giovambattista, P. G. Debenedetti and P. J. Rossky, *J. Phys. Chem. B*, 2007, **111**, 9581–9587.
46 F. Lin, X. Meng, M. Mertens, P. Cool and S. Van Doorslaer, *Phys. Chem. Chem. Phys.*, 2014, **16**, 22623–22631.
47 A. Pivtsov, M. Wessig, V. Klovak, S. Polarz and M. Drescher, *J. Phys. Chem. C*, 2018, **122**, 5376–5384.
48 M. Wessig, M. Drescher and S. Polarz, *J. Phys. Chem. C*, 2013, **117**, 2805–2816.
49 R. P. Mason, C. F. Polnaszek and J. H. Freed, *J. Phys. Chem.*, 1974, **78**, 1324–1329.
50 J. W. Stucki, W. L. Banwart and eds., *Advanced Chemical Methods for Soil and Clay Minerals Research, NATO Advanced Study Institutes Series: Series C, Mathematical and Physical Sciences*, Vol. 63, Springer Reidel: Boston, 1980.
51 R. S. de Biasi and A. A. R. Fernandes, *J. Phys. C: Solid State Phys.*, 1983, **16**, 5481–5489.
52 M. F. Ottaviani, M. Garcia-Garibay and N. J. Turro, *Colloids Surf., A*, 1993, **72**, 321–332.
53 B. Dzikovski, D. Tipikin, V. Livshits, K. Earle and J. Freed, *Phys. Chem. Chem. Phys.*, 2009, **11**, 6676–6688.
54 Y. Liu, *J. Chem. Eng. Data*, 2009, **54**, 1981–1985.
55 R. Ocampo-Perez, R. Leyva-Ramos, J. Mendoza-Barron and R. M. Guerrero-Coronado, *J. Colloid Interface Sci.*, 2011, **364**, 195–204.
56 N. Singh and C. T. Campbell, *ACS Catal.*, 2019, **9**, 8116–8127.
57 M. Keiluweit and M. Kleber, *Environ. Sci. Technol.*, 2009, **43**, 3421–3429.
58 W. M. Haynes, D. R. Lide and T. J. Bruno, *CRC Handbook of Chemistry and Physics, 97th edn, Vol. 2016–2017*, CRC Press, 2017.
59 I. Płowaś, J. Świergiel and J. Jadżyn, *J. Chem. Eng. Data*, 2013, **58**, 1741–1746.
60 H. E. Hoydonckx, W. Van Rhijn, D. E. De Vos and P. A. Jacobs, *Ullmann's Encyclopedia of Industrial Chemistry*, 2007, **16**, 285–313.